IEEE Open Journal of
Antennas and Propagation

Received 29 July 2021; revised 13 September 2021; accepted 27 October 2021. Date of publication 12 November 2021; date of current version 9 December 2021.

Digital Object Identifier 10.1109/OJAP.2021.3127631

Deployable Rigid-Flexible Tightly Coupled Dipole Array (RF-TCDA)

MAXENCE CARVALHO (Graduate Student Member, IEEE), AND JOHN L. VOLAKIS (Life Fellow, IEEE)

Department of Electrical and Computer Engineering, Florida International University, Miami, FL 33174, USA

CORRESPONDING AUTHOR: M. CARVALHO (e-mail: mcarvalh@fiu.edu)

This work was supported by the Air Force Office of Scientific Research under Grant FA9550-19-1-0290.

ABSTRACT An origami-based Tightly Coupled Dipole Array (TCDA) is proposed for small satellite applications. The array is formed by a two-layered structure using rigid and flexible substrates to enable accordion-like folding. The proposed TCDA operates across 0.4-2.4 GHz with VSWR < 3 at broadside and across 0.6-2.4 GHz with VSWR < 3 when scanning down to 45° in the E-, D-, and H-plane. An 8×8 prototype was fabricated using Kapton Polyimide and FR4 and tested to verify the bandwidth and gain of the origami array. The fabricated prototype was demonstrated to be packable, low-profile, and lightweight (only 1.1kg). Notably, when packed, the array has a one-dimensional size reduction of 75%. As will be discussed, the packing compression is made possible by eliminating vertical PCB boards and incorporating the balun feeds within the dipole layer. To our knowledge, this is one of the first foldable, low profile, and low-scanning ultra-wideband arrays in the literature.

INDEX TERMS Tightly coupled dipole array (TCDA), ultra-wideband (UWB) array, origami, rigid-flexible, cubesat.

I. INTRODUCTION

CUBESATS have become increasingly important for space applications due to their size and low deployment costs [1]–[2]. Concurrently, there is strong interest in developing deployable and packable antenna apertures for small satellites. The latter include minisatellites (100-500kg), microsatellites (10-100kg), nanosatellites (1-10kg), picosatellites (0.1-1kg), and femtosatellites (<0.1 kg). The growth of Low Earth Orbit (LEO) missions and planned Moon and Mars missions implies a strong demand for CubeSat High Gain Antennas (HGA). Already packable apertures such as mesh reflectors, inflatable antenna arrays, reflectarrays, and membrane arrays have been considered for CubeSats [3]. Reflector antennas are widely used for high-gain spacecraft antennas as they deliver high efficiency and polarization diversity. Notably, efforts have focused on developing parabolic antennas for CubeSats [4]. For instance, in [5], a 0.5 m L-Band deployable mesh reflector was presented. The reflector can be stored in a small volume of 10 cm × 10 cm × 16 cm (1.5U) inside a 3U CubeSat bus. Some of these mesh reflectors employ closely spaced foldable ribs. However, these ribs constrain reflectors folding to avoid cross-axis torques. As such, their packing complexity increases to ensure that no damage to the joints occurs.

To reduce the packing complexity of mesh reflectors, a wrap-around packing technique was proposed for S-Band applications in [6]. This technique considerably reduces the dish mass (<1 kg) and provides excellent packing efficiency. However, the design uses thin, flexible ribs that merely hold the mesh in place when deployed. Consequently, this type of mesh reflector suffers from poor surface roughness, diminishing its peak directivity.

Deployable reflectarrays (RA) constitute a compact alternative to deployable mesh reflectors. The latter are usually adapted to smaller CubeSats, but their narrow bandwidth is a limitation. Further, they typically have lower efficiencies ($< 50\%$) than reflectors and may be sensitive to temperature variations [7]–[8].

Membrane antennas and membrane arrays are extremely lightweight options [9]–[11]. They allow for compact stowage and low area densities of less than 2 kg.m^2. In the deployed configuration, the membranes are tensioned using cables typically attached to hoop structures. However, the wrapping of the antennas creates creases, wrinkles, and

ripples that form faulty handling and tension. As a result, they suffer from poor surface accuracy, reducing their peak gain [12]–[13].

To further improve stowage efficiency, inflatable antennas for CubeSat have also been proposed. In [14], an inflatable S-Band (2.4 GHz) reflector is proposed. This reflector has minimal volume storage of 0.6U (for a 3U CubeSat). However, vacuum tests concluded that residual air in the antenna might cause it to inflate unexpectedly prior to deployment. This significantly affects the Technology Readiness Level (TRL) of the latter. Further, the aluminized Mylar surfaces retain wrinkles, causing surface roughness even at S-Band frequencies. Alternatively to the aforementioned antennas, a narrowband Rigid-Flexible Antenna Array (RFAA) was presented in [15]. This array consists of a combination of flexible Pyralux layers and rigid PCB.

With the goal of developing ultra-wideband (UWB) and packable HGA for CubeSats, in this paper, we propose a class of origami-based Tightly Coupled Dipole Arrays (TCDAs), known to deliver optimal bandwidths [16]. To date, Origami phased arrays have yet to be considered. Previous TCDA arrangements have been formed using the egg-crate configuration, but these egg-crate TCDA structures are not suitable for CubeSats. Further, their vertical baluns make them unsuitable for folding. With this in mind, this paper proposes a Rigid-Flexible TCDA (RF-TCDA). The proposed incorporation of origami structural properties into classic TCDAs leads to highly packable and readily unfoldable arrays. The proposed RF-TCDA is comprised of two rigid-flexible strata whose displacements are constrained by nylon screws (Fig. 1). The developed array operates across 0.4-2.4 GHz with VSWR < 3 at broadside and across 0.6-2.4 GHz with VSWR < 3 when scanning down to 45° in the E-, D-, and H-plane. Notably, and equally important, the fabricated design weighs only 1.1kg and is extremely low-profile ($0.067\lambda_{low}$, where λ_{low} is the wavelength at the lowest frequency of 400 MHz). When packed, the entire array has a one-dimensional size reduction of 75% and fits in a volume of 51 cm × 12.8 cm × 10.5 cm. Additionally, the paper also presents a deformation study of the fabricated array. Precisely, single- and double-curvature distortions are characterized and studied.

This communication is organized as follows. Section II introduces the design of the proposed accordion-like array. Section III presents the fabrication details, and measurements data for an 8×8 prototype. Section IV discusses the array's performance under structural deformations, and Section V proposes further improvements. In summary, the proposed design provides a proof of concept for the design and fabrication of lightweight, deployable, and UWB apertures for small satellites.

II. ARRAY DESIGN AND SIMULATION

A. FOLDABLE UNIT CELL DESIGN

As depicted in Figs. 1 and 2, the dipoles, feed structure, and capacitive overlapping pads were placed on a Kapton ($\epsilon_r = 3.4$) substrate of thickness $t_k = 0.225$ mm, interposed

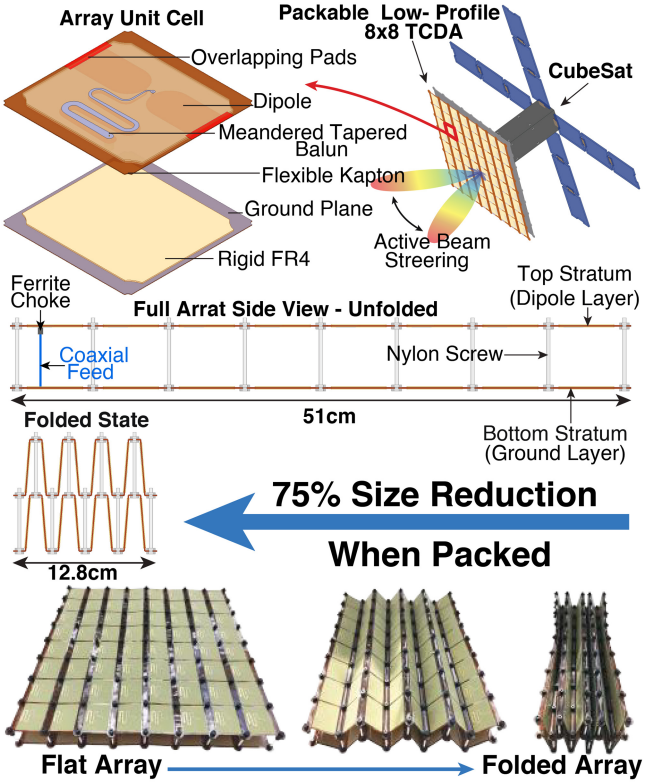

FIGURE 1. Proposed deployable Rigid-Flexible Tightly Coupled Dipole Array (RF-TCDA) unit cell details. Nylons screws are used to constrain the displacement of both layers when the array folds. When packed, the array shows a one-dimensional size reduction of 75%.

between two FR4 layers ($\epsilon_r = 4.4$) of thickness $t_{FR4} = 0.225$ mm. The FR4 substrates serve as stiffeners to keep RF consistency. Notably, the flexible Kapton layer is perforated at the edges to create ease for foldability. As depicted in Fig. 2 (right-most graphic), the dipole arms are etched at the bottom part of the lower FR4 stiffeners. The overlapping capacitive strips are placed at the top of the Kapton and create the current sheet effect. As is usually the case with TCDAs (see Fig. 2), the capacitive coupling is controlled by the length (L_c) and width (W_c) of the overlapping metal pads across the dipole ends. Importantly, the structure has a small thickness of less than $0.067\lambda_{low}$ from the ground to the dipole surface, with λ_{low} being the wavelength at 400 MHz. Of importance is that the FR4 stiffeners must be designed to ensure folding at the perforated Kapton edges. Nylons screws are also used to constrain the displacement of the layers when the array folds. Notably, this is the first deployable TCDA designed on foldable substrates.

The proposed TCDA unit cell is a particular case of the Miura-ori TCDA architecture previously proposed by Carvalho and Volakis in [17]. As shown in Fig. 3, θ_m is the angle formed by the xy-plane and each face of the Miura fold. Notably, the ground and dipole layers fold simultaneously to avoid breaking. Specifically, an offset was added to the unit cell to accommodate for the substrate thickness and make room for the vertical nylon screws presented in Fig. 2 (left-most graphic, while folding). The dipoles (in

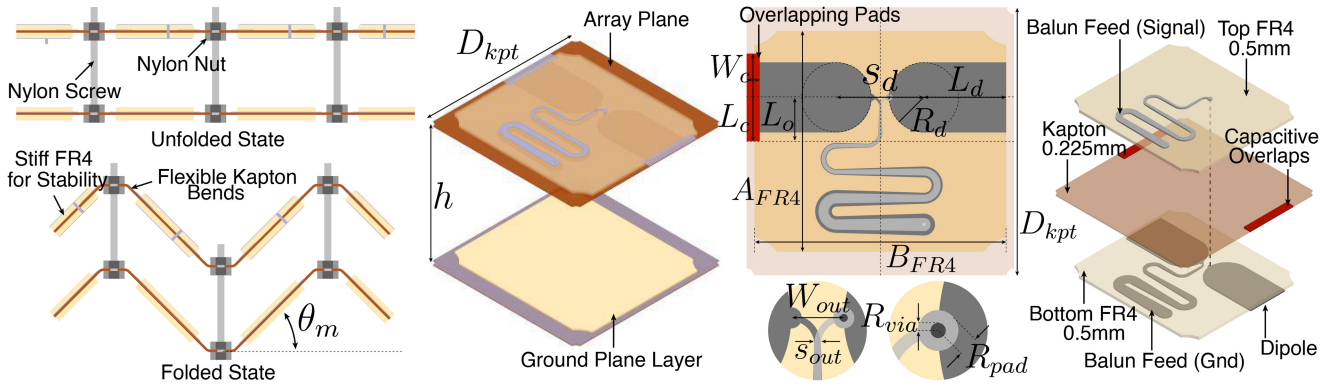

FIGURE 2. Proposed deployable Rigid-Flexible Tightly Coupled Dipole Array (RF-TCDA) unit cell details. Nylons screws are used to constrain the displacement of both layers when the array folds. When packed, the array shows a one dimensional size reduction of 75%.

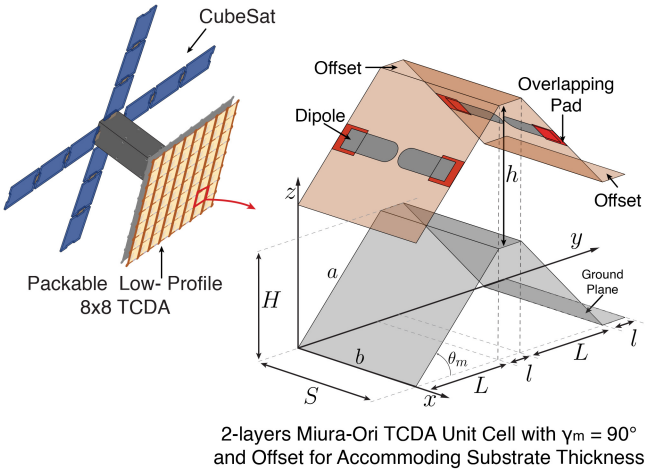

FIGURE 3. Simplified version of the proposed accordion TCDA unit cell. The accordion unit cell is adapted from the Miura fold whose acute angle γ_m is set to its maximum value of $\gamma_m = 90°$.

grey) and the overlapping pads (in red) are printed along the x-direction of the flat radiating sheet. When folding, radiation remains in the horizontal polarization with minimal intended cross-polarization distortion. When flat, the distance between the ground plane and the dipole sheet remains $h = \lambda_{high}/2.2$, where λ_{high} is the wavelength at the highest operating frequency. This spacing offers good low-frequency performance and excludes ground plane shorts for optimal bandwidth [18]. Furthermore, the inter-element spacing is based on the highest operating frequency. It is remarked that, for a flat TCDA surface, the unit cell is such that $2\left[L(0, \gamma_m) + \ l\right] = \lambda_{high}$, where l is the offset length.

As noted, while folding, the proposed TCDA unit cell fits in a cuboid of volume $S \times 2(L + l) \times (H \ + \ h)$, where (see Fig. 3):

$$H(\theta_m) = a\sin\theta_m = \left(\frac{\lambda_{high}}{2} - 1\right)\sin\theta_m \tag{1}$$

$$S(\theta_m) = b = D_{pkt} = \frac{\lambda_{high}}{2} \tag{2}$$

$$L(\theta_m) = a\cos\theta_m = \left(\frac{\lambda_{high}}{2} - 1\right)\cos\theta_m. \tag{3}$$

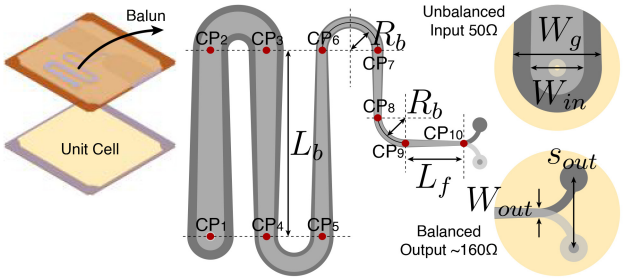

FIGURE 4. Meandered tapered balun. The balun includes a smooth transition from an unbalanced input of 50 Ω to a pair of balanced outputs, each exhibiting ~ 160 Ω, viz. the input impedance of the overlapping dipoles.

B. MEANDERED TAPERED BALUN

To ensure that the TCDA bandwidth is retained, a new tapered balun feed is proposed and realized. Particularly, it is important to reduce the balun length via meandering. For our case, we chose the microstrip line that feeds the overlapping dipoles to be tapered as follows (see Fig. 4):

$$W_{Feed}{}_{CP_n}^{CP_{n+1}} = \frac{W_{out} - W_{in}}{D_{total}} D(CP_n, CP_{n+1}) + W_{in} \tag{4}$$

$$W_{Gnd}{}_{CP_n}^{CP_{n+1}} = \frac{W_{out} - W_{in}}{D_{total}} D(CP_n, CP_{n+1}) + W_g \tag{5}$$

$$D_{total} = \sum_{n=2}^{10} D(CP_n, CP_{n+1}) \tag{6}$$

Referring to Fig. 4, CP_n, $n \in [\![1, \ N]\!]$ are the control points for the parametric equation. In the above, W_{in} is the width of the microstrip at CP_1, W_g is the width of the microstrip ground at CP_1, and W_{out} is the microstrip/ground width at CP_{10}. Also, $D(CP_n, CP_{n+1})$ is the Euclidean distance between CP_n and CP_{n+1}, and D_{total} refers to the overall balun length. The novel balun is depicted in Fig. 4. We remark that this balun delivers more than 15 dB isolation between the common and differential modes across the entire band. Concurrently, the input impedance was tapered from 50 Ω to ~ 160 Ω at the dipole aperture.

The final dimensions of the fabricated balun are: L_b = 20 mm, R_b = 3 mm, L_f = 6 mm, s_{out} = 4 mm, W_{out} = 0.5 mm, W_{in} = 3 mm, W_g = 5 mm.

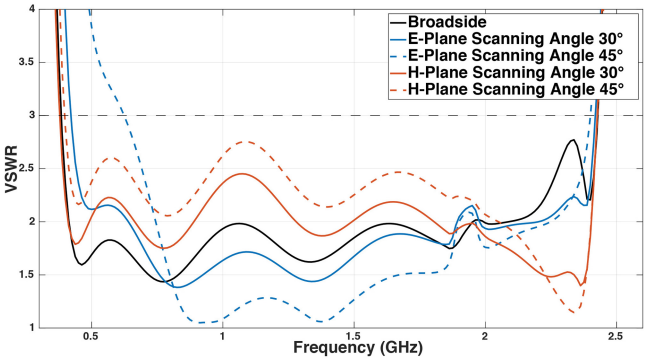

FIGURE 5. Simulated active VSWR at broadside for the infinite array and while scanning in the E- and H-plane at 30° and 45° from broadside.

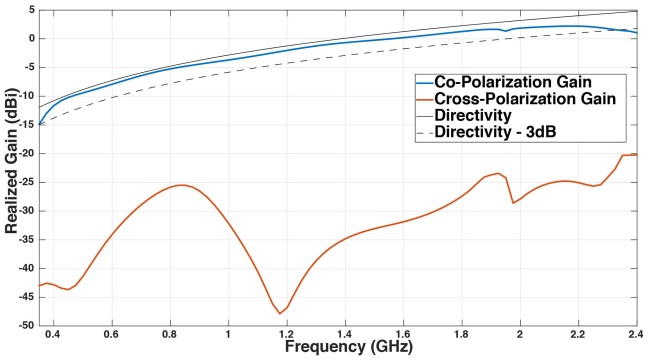

FIGURE 6. Simulated broadside gain per unit cell versus unit cell directivity $4\pi A/\lambda^2$.

C. INFINITE ARRAY ANALYSIS

An infinite array simulation was realized using the commercially available software Ansys HFSS. The proposed unit cell was simulated in the presence of a coaxial cable and a ferrite-choke to avoid common-mode resonances due to currents on the outer layer of the coaxial cable. As seen in Fig. 5, the infinite array simulations show that the proposed RF-TCDA with the integrated balun presented in Fig. 4 operates across 0.4-2.4 GHz with VSWR < 3 at broadside. At 45° (E- and H-plane), with VSWR < 3, the RF-TCDA operates across 0.6-2.4 GHz. Notably, reduced performance is expected when scanning at low angles due to variations in the dipole array impedance [19].

The addition of FSS superstrates (WAIM-FSS) certainly improves scanning at low angles by addressing impedance mismatches [20]–[21]. However, such designs require more complex fabrication and the incorporation of additional horizontal boards. The corresponding simulated co- and cross-polarization gains curves are given in Fig. 6. As seen, the co-polarization gain closely follows the theoretical $4\pi A/\lambda^2$ aperture reference (where A is the unit cell area). It is worth mentioning that the efficiency drops after 2 GHz, attributed to the ferrite choke placed at the coaxial cable feed. Nevertheless, the overall radiation efficiency is 85% on average. The final design dimensions of the unit cell are given in Table 1.

TABLE 1. Unit cell dimensions presented in Fig. 2.

Parameters	Dimensions (mm)	Parameters	Dimensions (mm)
h	50	A_{FR4}	50.3
W_c	3	B_{FR4}	57.6
L_c	20	t_{FR4}	0.51
L_o	10	L_b	20
R_d	8	R_b	3
L_d	18.7	L_f	6
s_d	4	W_g	5
R_{via}	0.3	W_{in}	3
R_{pad}	0.8	W_{out}	0.5
D_{kpt}	61	s_{out}	4
t_k	0.225		

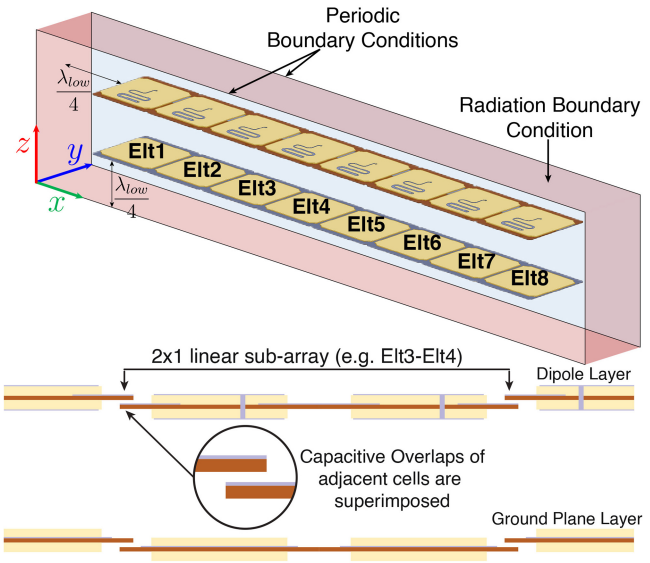

FIGURE 7. Simulation setup for the 8 x 1 semi-infinite array. The capacitive overlaps of adjacent cells are superimposed.

D. SEMI-INFINITE ARRAY SIMULATIONS

To reduce the rigid-flexible fabrication cost, we considered a modular fabrication approach comprised of smaller sub-arrays. This was done because the manufacturing cost of Kapton polyimide and rigid PCBs rapidly increases with the board size. This is because the flexible Kapton is manufactured in tapes that are long but very narrow. Typical Kapton tapes are used for flexible electrical connections in robotics and small antennas, viz. not suitable for large square apertures. The employed simulation model considered the Kapton tape usage for fabrication. Specifically, the simulation model shown in Fig. 7 employs eight array elements lying in the x-direction and uses periodic boundary conditions (PBC) along the y-direction. The radiation or absorbing boundary condition is placed at a $\lambda_{low}/4$ distance from the top and bottom of the RF-TCDA. In the semi-infinite simulation, consecutive elements we paired. Precisely, we paired the first element with the second, the third with the fourth, etc. For the junction between each pair, we extended the overlapping pads and superimposed them.

From the above, we note that the array elements show higher active VSWRs, particularly at lower frequencies. Such characteristics are well known for smaller ultra-wideband

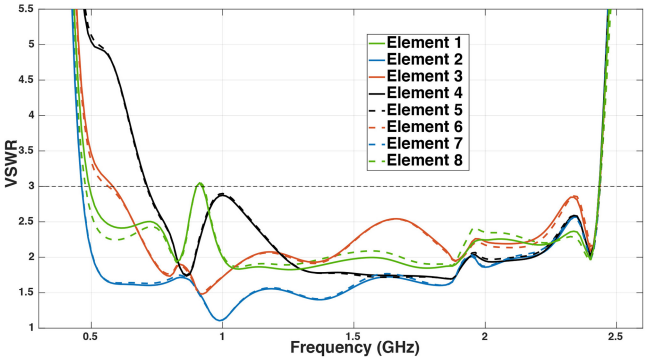

FIGURE 8. Simulated active VSWRs of the 8 × 1 array presented in Fig. 7.

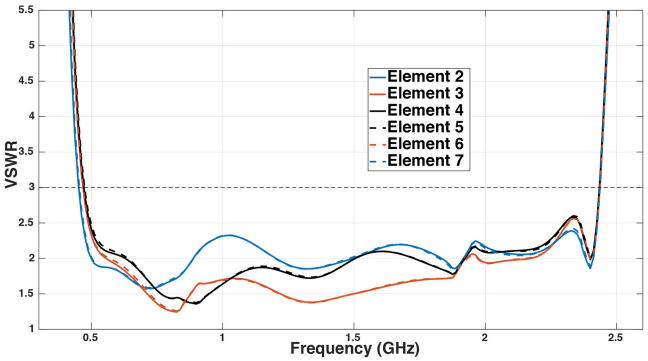

FIGURE 9. Simulated active VSWRs of the 8 × 1 array presented Fig. 7 with tapered elements.

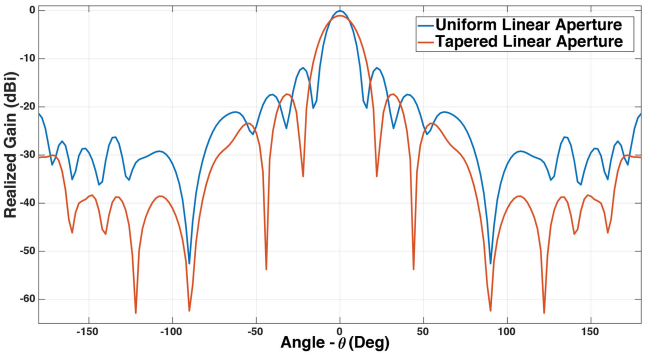

FIGURE 10. Normalized simulated realized gain pattern of the 8 × 1 array for uniform and tapered excitations at 2.4 GHz.

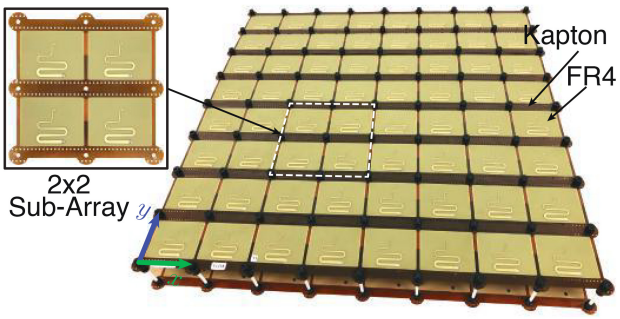

FIGURE 11. Photo of the fabricated 8 × 8 RF-TCDA prototype.

apertures [22]–[23]. Precisely, edge elements do not behave like center elements, as would be expected for infinite array simulations. For higher frequencies, the VSWR of the elements matches the infinite simulation.

A solution to optimize the matching of the finite array elements was proposed in [24] using characteristic mode analysis. By doing so, one can find the optimum element feed taper. This approach leads to better VSWR and concurrently good radiation efficiency. However, this method requires the excitation of several modes of the apertures to match the array over a wide range of frequencies. A simpler solution is to employ a cosine tapering function. To assess this statement, a cosine taper was applied to the 8×1 linear array with the center elements and the edge elements having the maximum and minimum excitation amplitude, respectively. From Fig. 9 we observe a much-improved matching at the lower frequencies.

The simulated gains for the uniformly excited and the tapered 8×1 linear arrays at 2.4 GHz are compared in Fig. 10. As expected, the cosine tapering of the excitation leads to a widening of the 3 dB beamwidth (θ_{3dB}) and a gain reduction of 1 dB.

III. PROTOTYPE FABRICATION AND MEASUREMENTS

A. RIGID-FLEXIBLE ARRAY FABRICATION

To assess the characteristics of the designed RF-TCDA, an 8×8 prototype was fabricated (see Fig. 11). Following the study presented in Section II, the assembly of this prototype was done using sixteen 2×2 sub-arrays. Also, of importance is that the stiffeners must be designed to ensure folding at the perforated Kapton edges (see Fig. 12a). Nylons screws were also used to constrain the displacement of both strata while folding. Further, the flexible Kapton layer was perforated at its edges for foldability ease. As shown in Figs. 12a the meandered baluns and the dipoles are etched on the FR4 stiffeners while the overlapping capacitive strips are placed at the top of the Kapton sheet. We remark that the Kapton substrate sheet and the capacitive dipole overlaps were extended to ensure that the sub-arrays exhibit the same capacitive overlap when the TCDA is assembled to form the 8×8 array depicted in Fig. 11.

As can be realized, when the 2×2 sub-arrays are assembled, their height with respect to the ground plane was adjusted using the nylon bolts at the junctions of the unit cell. This ensures the planarity of the 8×8 TCDA.

B. ACTIVE IMPEDANCE MEASUREMENTS

The assembled prototype shown in Fig. 11 was used to carry out active impedance measurements using the Keysight N5222B Vector Network Analyzer (VNA). For measurements, the mutual coupling with neighboring elements was also quantified and combined with the return loss of the antenna elements under test. This was done to compute the active S-parameters of the pqth element using an expression that accounts for the cosine tapering of the excitation [25].

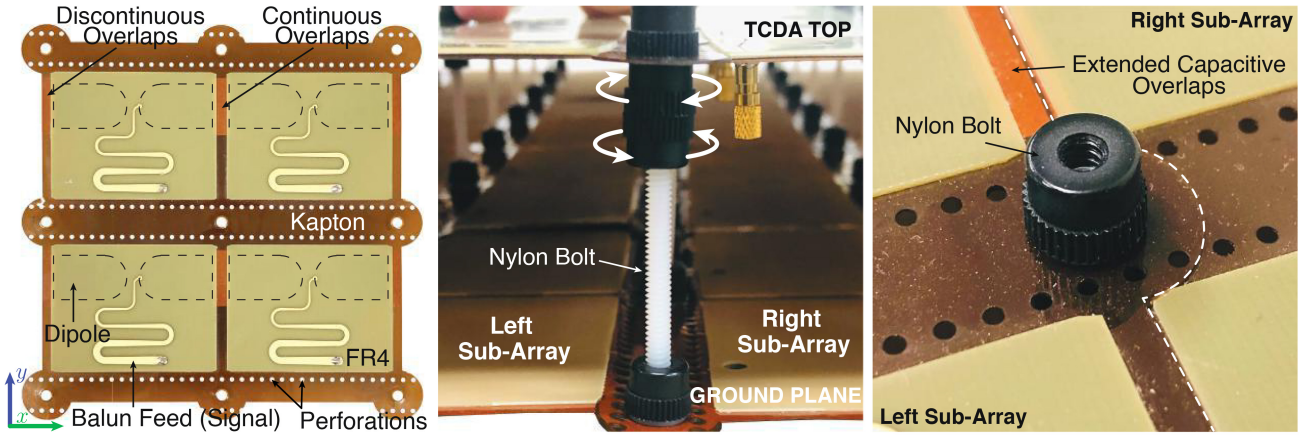

FIGURE 12. Fabrication details of the 2 × 2 sub-arrays, forming the 8 × 8 RF-TCDA. (a) Top view of a 2 × 2 sub-array, (b) Side view of the array elements, (c) Top view at the junction of the 2 × 2 sub-arrays showing the Nylon bolt used for adjustment.

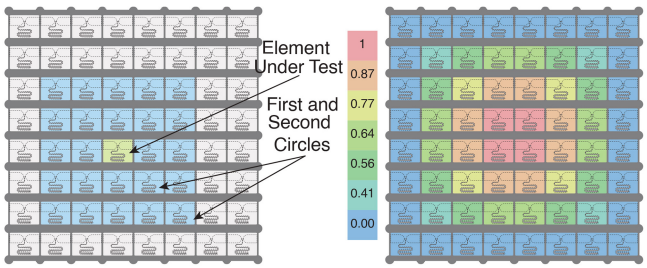

FIGURE 13. Active S-parameters measurements set-up. In this specific example, the element under test is ($p = 4, q = 4$) (light green, left-graphic). The first and second surrounding circles away from the (4,4) element are used for computing the VSWR using the cosine taper presented on the right graphic.

Specifically, the active reflection coefficient of the pqth element within the array was determined from

$$\Gamma_{p,q}(\theta,\phi) = \frac{\sum_{m=1}^{M}\sum_{n=1}^{N} V_{mn} S_{mn,pq} e^{-j\mathbf{k}.(\mathbf{p_{mn}}-\mathbf{p_{pq}})}}{V_{pq}} \quad (7)$$

In the above, M and N are the number of elements along the x- and y- directions, respectively, (θ, ϕ) is the array scan direction. Also, V_{mn} is the complex excitation of the array's mnth element, $\mathbf{p_{mn}}$ is the position vector expressed in the global coordinate system $(\mathbf{x}, \mathbf{y}, \mathbf{z})$, and $\mathbf{k}$ refers to the propagation vector. As usual, $S_{mn,pq}$ refer to the measured S-parameters between the mnth and pqth elements. As shown in Fig. 13 (left-most graphic), the measurements of the VSWR of the elements used the S-parameters up to two elements away from the active one. Further, from (7), the active VSWR was calculated accounting for the unequal complex excitations.

The measured active VSWR in the E-, D- and H-plane of a central element is shown in Fig. 14 and compared to the infinite array simulations. As seen, the measurements have good agreement with the infinite array simulations. Indeed, the measured prototype was shown to deliver the designed 6:1 bandwidth with VSWR < 3 from 0.4 GHz to 2.4 GHz at broadside. Great scanning agreement is also seen with some discrepancies at D/H-plane at $\theta = 45°$. The excitation tapering also contributed to lowering the input impedance of the elements under test [22]. Notably, a near 6:1 bandwidth from 0.45 GHz to 2.4 GHz is observed when scanning down to $\theta = 45°$ in the E-, D- and H-plane.

C. FAR-FIELD MEASUREMENTS

Gain measurements were conducted in a near-field anechoic chamber across 0.65-2.4 GHz. Doing so, the measured broadside gain versus frequency for a central element is shown in Fig. 15. The theoretical aperture gain $4\pi A/\lambda^2$ is also overlaid as a reference. We observe that the center elements gain closely tracks the simulated realized gain, demonstrating the success of this multifaceted ultra-wideband array design.

To account for finite array effects of the TCDA, the measured broadside gain of an 8 × 1 elements linear array was also measured and shown in Fig. 16. These measurements were conducted using an 8-ways power divider with subsequent post-processing, including cables and power divider losses. Notably, the gain measurements for this linear TCDA account for finite effects and all couplings among the elements. We note a reduced gain and higher sidelobes due to phase and amplitude imbalance from the power divider used (DC Pass model ZN8PD1−63W−S+). An increased 3 dB beamwidth θ_{3dB} and higher sidelobe levels (SLL) are typical characteristics of these variations [26].

The gain patterns at 800 MHz, 1.8 GHz, and 2.2 GHz are presented in Fig. 17 in the E- and H-plane cuts, respectively. The theoretical ideal element pattern is also included for reference. Notably, the measured co-polarization patterns closely follow both simulations and the theoretical aperture gain of $4\pi A\cos\theta\ /\lambda^2$. As expected, the beamwidth is wider at 800 MHz since the array element is only $\lambda/6$ in aperture at 800 MHz. Overall, finite array measurements are in good agreement with some discrepancies in the cross-polarization levels. The latter is mostly attributed to the difficulty in achieving perfect alignment during

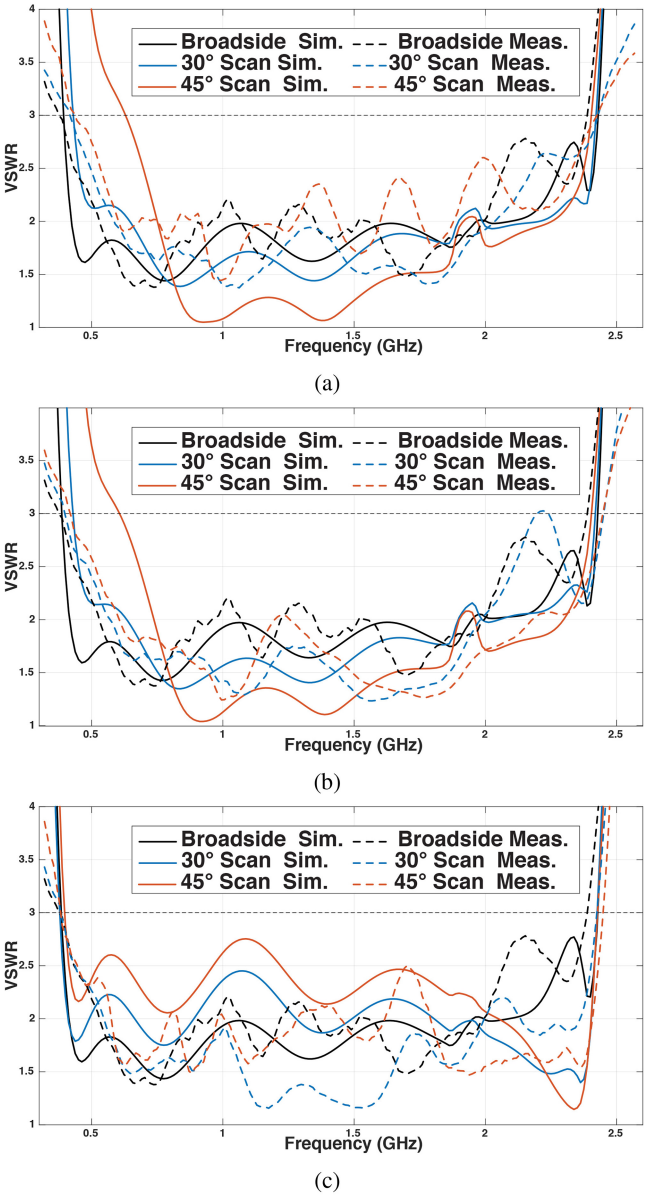

FIGURE 14. Measured and simulated active VSWR of a center element at broadside, $\theta = 30°$ and $\theta = 45°$ scans. (a) E-Plane, (b) D-Plane, (c) H-Plane.

fabrication and measurements. Additionally, the meandered structure of the balun was found to be responsible for the increased H-plane cross-polarization. When scanning, the balun meandering creates y-oriented TE currents, affecting the cross-polarization. This reduced polarization purity can be seen in Figs. 15 and 17a around 800 MHz. Typically, the observed pattern ripples are due to the finite size of the array. Also, the small pattern asymmetries are due to small asymmetries in the fabricated elements.

IV. PERFORMANCE UNDER STRUCTURAL DISTORTION

In this section, we consider the 8×8 array prototype presented in Section III. The fabricated 8×8 array prototype shows mechanical deformations inherent to its rigid-flexible structure. As presented in [26]–[27], mechanical distortions

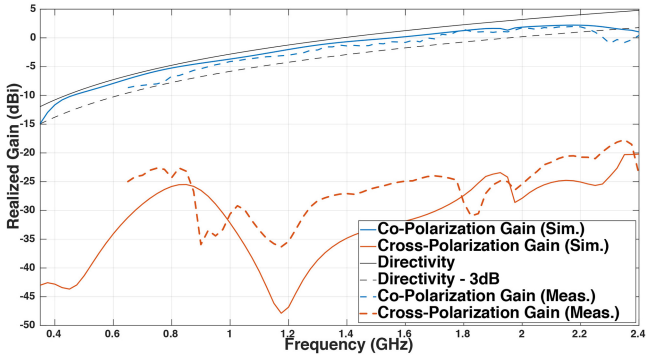

FIGURE 15. Simulated and measured realized broadside gains of a central unit cell.

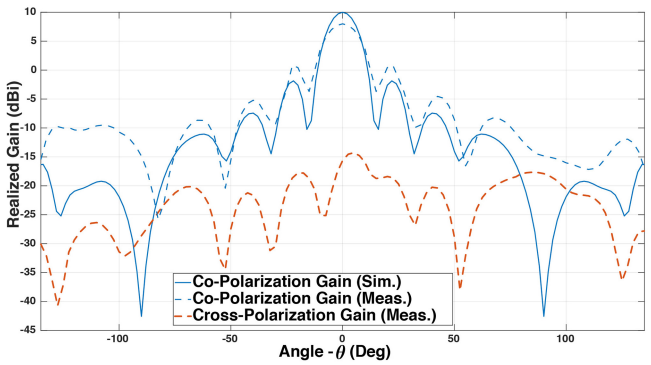

FIGURE 16. Measured broadside co-polarization gain of one central row of the fabricated prototype at 2.4 GHz (8 elements).

can significantly impact the gain and SLL. To characterize these deterministic deformations, we study the influence of single and double curvature distortions, as seen in Figs. 18 and 21. In the following, we consider chain-like distortions. These appear naturally when flexible structures are held by their extremities.

A. SINGLE-CURVATURE DISTORTION

In the single-curvature mode, the 8×8 array prototype is bent only along the y-direction. As seen in Fig. 18, the distortion is such that the elements at the x-oriented edges of the array are symmetrically elevated to maximum vertical amplitude, z_{max}. Also, we assume that the distortions do not cause changes in the x and y element positions. That is, the array elements phase centers are altered as follows:

$$\begin{cases} x_m = (2m-1)\frac{\lambda_{high}}{4} \\ y_n = (2n-1)\frac{\lambda_{high}}{4} \\ z_{mn} = z_{max}(\cosh(A(y_n - y_0)) - 1) \end{cases} \tag{8}$$

In the above, z_{max} is the maximum vertical distortion amplitude, and $y_0 = (y_1 + y_N)/2$ is the center of symmetry, even during the distortion. Also, A is a coefficient characterizing the deformation. Notably, single-curvature deformations appear naturally when the array is fixed at the edges corresponding to $y = y_1$ and $y = y_N$. Therefore, in this case

$$A = \frac{2\text{acosh}(2)}{y_1 - y_N} \tag{9}$$

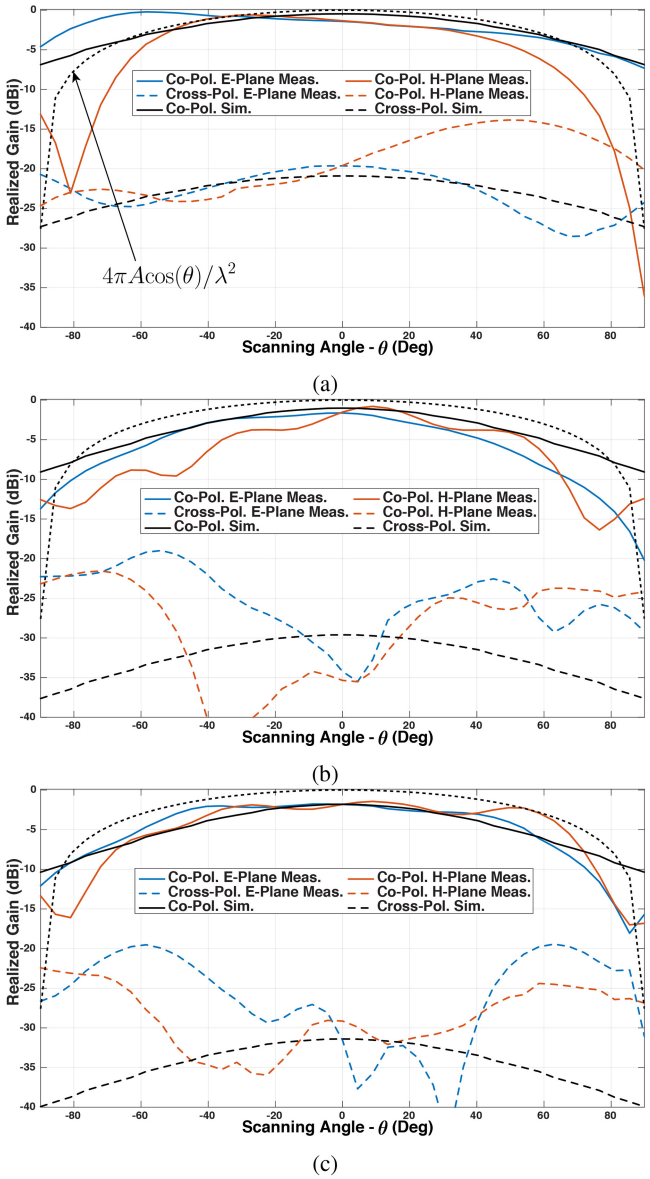

FIGURE 17. Measured array pattern with a center element of the 8 × 8 array being excited. Patterns are given in E- and H-plane with comparison to infinite array simulation at: (a) 800 MHz (b) 1.8 GHz (c) 2.2 GHz.

Denoting the array elements as$(m, n) \in [\![1, N]\!] \times [\![1, M]\!]$, assuming that all the element patterns remain identical, and without considering inter-element coupling, the far-field radiation pattern can be expressed as

$$f(\theta, \phi) = \sum_{m=1}^{M} \sum_{n=1}^{N} I_{mn} e^{j\mathbf{k}.\mathbf{p_{mn}}} \tag{10}$$

In the above, N and M denote the numbers of elements in the x- and y-directions, respectively, and I_{mn} is the complex excitation of the mn$^{\text{th}}$ element. Also, $\mathbf{p_{mn}} = [x_m, y_n, z_{mn}]$ is the position vector of the mn$^{\text{th}}$ element, and $\mathbf{k}$ refers to the propagation vector in the global coordinate system $(\mathbf{x}, \mathbf{y}, \mathbf{z})$. Given that $\mathbf{p_{mn}}$ is arbitrary, (10) applies to any deformation

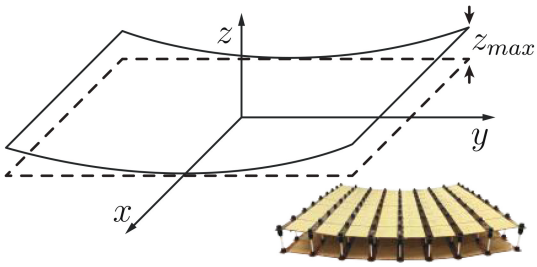

FIGURE 18. Fabricated array prototype under single-curvature deformation.

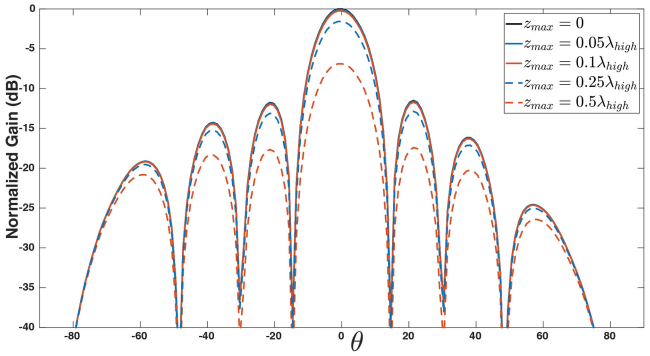

FIGURE 19. Normalized E-Plane array pattern for the 8 × 8 array prototype at 2.4 GHz under single-curvature distortion.

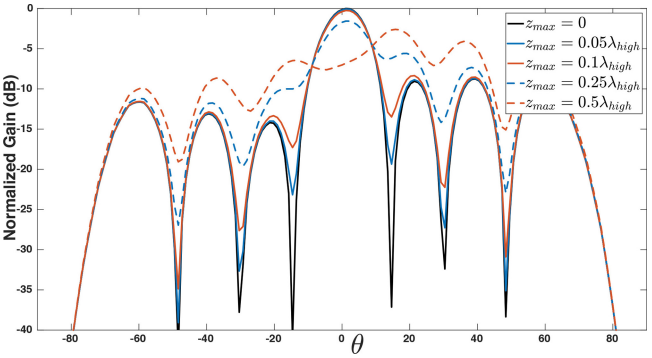

FIGURE 20. Normalized H-Plane array pattern for the 8 × 8 array prototype at 2.4 GHz under single-curvature distortion.

of the array. For a fixed direction (θ, ϕ), $\mathbf{k}$ is given by

$$\mathbf{k} = k[u,\ v,\ w] = \frac{2\pi}{\lambda}[u,\ v,\ w] \tag{11}$$

where, as usual, $u = \sin\theta\cos\phi$, $v = \sin\theta\sin\phi$, $w = \cos\theta$, and λ is the operational wavelength.

Using (8)-(11) we can rewrite $f(\theta, \phi)$ as

$$f(\theta, \phi) = \sum_{m=1}^{M} \sum_{n=1}^{N} I_{mn} e^{jk(x_m u + y_n v + z_{mn} w)} \tag{12}$$

The above pattern expression was used to compute the far-field pattern of the distorted array as depicted Fig. 18. This far-field pattern was computed at 2.4 GHz and for different values of $0 \leq\ z_{max} \leq\ 0.5\lambda_{high}$.

The calculated gain pattern in the E- and H-plane cuts are presented in Figs. 19 and 20, respectively. It is seen that the influence of distortions is more pronounced in

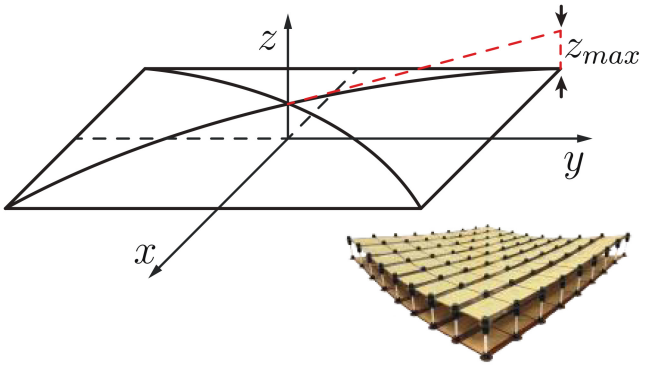

FIGURE 21. Fabricated array prototype under double-curvature deformation.

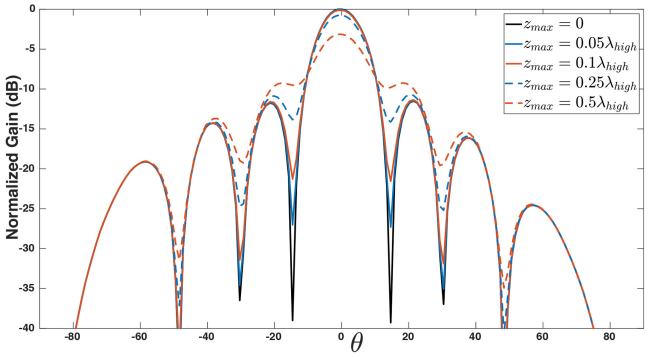

FIGURE 22. Normalized E-Plane array pattern for the 8 × 8 array prototype at 2.4 GHz under double-curvature distortion.

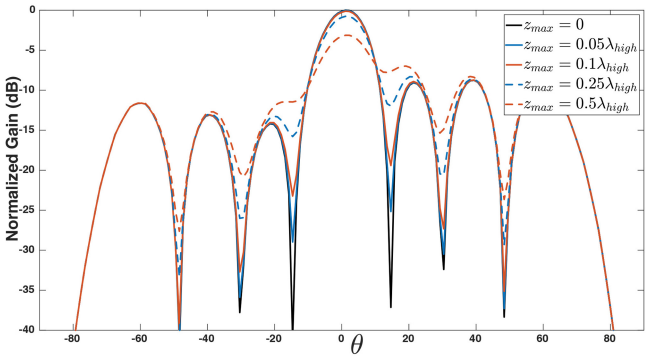

FIGURE 23. Normalized H-Plane array pattern for the 8 × 8 array prototype at 2.4 GHz under double-curvature distortion.

the H-plane. This was expected as the deformation occurs along the y-direction. We also observe degradation in the gain pattern, depending on the value of z_{max}. Asymmetry is also noticed in the H-plane but is due to the embedded pattern used for the computation. The fabricated 8×8 prototype exhibits a maximum deformation amplitude of $z_{max} = 0.2\lambda_{high}$ when supporting its weight. Of importance is that the rigid-flexible TCDA structure drastically reduces deformation. Deformation is also limited due to the employed FR4 stiffeners preventing the array from bending.

B. DOUBLE-CURVATURE DISTORTION

The 8×8 array prototype was also evaluated when double surface distortion occurs as in Fig. 21. This distortion is such that the corner elements are symmetrically elevated to a maximum vertical amplitude, z_{max}. In practice, the double-curvature deformation appears when the array is hanging by its corners. When distorted, the array element phase centers are given by:

$$\begin{cases} x_m = (2m-1)\frac{\lambda_{high}}{4} \\ y_n = (2n-1)\frac{\lambda_{high}}{4} \\ z_{mn} = z_{max}\left[f_1(x_m, y_n) f_2(x_m, y_n) - 1\right] \end{cases} \tag{13}$$

In the above, z_{max} is the maximum amplitude of the distortion, and $x_0 = (x_1 + x_M)/2$ and $y_0 = (y_1 + y_N)/2$ are the coordinates of the center of symmetry. Also, A and B are the coefficients characterizing the deformation and are given by:

$$A = B = \frac{2\sqrt{2}\text{acosh}(2)}{(x_1 - x_M) + (y_1 - y_N)} \tag{14}$$

Further, f_1 and f_2 are two chain-like curvature functions given by:

$$f_1(x_m, y_n) = \cosh\left(A\frac{(x_m - x_0) + (y_n - y_0)}{\sqrt{2}}\right) \tag{15}$$

$$f_1(x_m, y_n) = \cosh\left(B\frac{(x_m - x_0) - (y_n - y_0)}{\sqrt{2}}\right) \tag{16}$$

Using (13)-(16), we proceed to compute the far-field pattern of the curved array in Fig. 21. The corresponding patterns are given in Figs. 22 and 23, for the E- and H-plane cuts, respectively.

From Figs. 22 and 23, it is seen that the array curvatures affect the E- and H-plane patterns in the same manner. The side lobes are also affected. Notably, the fabricated 8×8 prototype had a maximum deformation amplitude of $z_{max} = 0.4\lambda_{high}$ when hanging at its corners. To mitigate deformation effects, aperture tapering can be used. Specifically, it was shown in [26] that a Gaussian tapering of the aperture leads to better SLL but some trade-offs in gain and beamwidth.

V. CONCLUSION AND REMARKS

A packable, low-profile, and low-scanning origami-based TCDA was proposed. This new class of RF-TCDAs was successfully demonstrated via measurements and shown to deliver the designed 6:1 bandwidth with a radiation efficiency of 85%, on average. The proposed rigid-flexible prototype operates across 0.4-2.4 GHz with VSWR < 3 at broadside and across 0.6-2.4 GHz when scanning down to 45°nand without additional FSS superstrates. Key to the design was the elimination of vertical PCB boards by using a balun feed within the dipole layer to achieve a rigid-flexible fabrication.

A study of the aperture's performance under structural distortion was given for practical considerations. It was noticed that when double-curvature occurs, the pattern deformation is evenly distributed between the E- and H-plane patterns. Such behavior is mostly due to the symmetry of such deformation. In summary, this paper provided a new

class of foldable UWB arrays suitable for future space-borne deployable antenna arrays.

REFERENCES

[1] E. Hand, "The rise of the CubeSat," *Science*, vol. 346, p. 1449, Dec. 2014. Accessed: May 21, 2021. [Online]. Available: https://science.sciencemag.org/

[2] E. Kulu. "Nanosats Database 2014–2021." [Online]. Available: https://www.nanosats.eu/ (Accessed: May 20, 2021).

[3] N. Chahat *et al.*, "Advanced CubeSat antennas for DeepSpace and earth science missions: A review," *IEEE Antennas Propag. Mag.*, vol. 61, no. 5, pp. 37–46, Oct. 2019.

[4] N. Chahat, R. E. Hodges, J. Sauder, M. Thomson, E. Peral, and Y. Rahmat-Samii, "Cubesat deployable Ka-band mesh reflector antenna development for earth science missions," *IEEE Antennas Propag. Mag.*, vol. 64, no. 6, pp. 2083–2093, Jun. 2016.

[5] M. Aherne, T. Barrett, L. Hoag, E. Teegarden, and R. Ramadas, "Aeneas—Colony I meets three-axis pointing," in *Proc. 25th Annu. Amer. Inst. Aeronaut. Astronaut. Utah State Univ. Conf. Small Satell.*, 2011, pp. 1–11.

[6] C. S. MacGillivray, "Miniature high gain antenna for CubeSats," in *Proc. CubeSat Developers Workshop*, San Luis Obispo, CA, USA, Apr. 2011.

[7] R. E. Hodges, N. Chahat, D. J. Hoppe, and J. D. Vacchione, "A deployable high-gain antenna bound for mars: Developing a new folded-panel reflectarray for the first CubeSat mission to mars," *IEEE Antennas Propag. Mag.*, vol. 59, no. 2, pp. 39–49, Apr. 2017.

[8] R. E. Hodges, D. J. Hoppe, M. J. Radway, and N. E. Chahat, "Novel deployable reflectarray antennas for CubeSat communications," in *Proc. IEEE MTT-S Int. Microw. Symp.*, 2015, pp. 1–4.

[9] F. Zhang, G. Yang, Y. Jin, F. Peng, and J. Mo, "Space-borne deployable P-band dual-circular-polarization flexible antenna array," *IEEE Antennas Wireless Propag. Lett.*, vol. 16, pp. 2529–2533, 2017.

[10] A. Moussessian *et al.*, "An active membrane phased array radar," in *IEEE MTT-S Int. Microw. Symp. Dig.*, 2005, pp. 1711–1714.

[11] P. A. Warren, J. W. Steinbeck, R. J. Minelli, and C. Mueller, "Large, deployable S-band antenna for a 6U CubeSat," in *Proc. 29th Annu. Amer. Inst. Aeronaut. Astronaut. UtahState Univ. Conf. Small Satell.*, 2015, pp. 1–7.

[12] J. Ruze, "The effect of aperture errors on the antenna radiation pattern," *Il Nuovo Cimento*, vol. 9, pp. 364–380, Mar. 1952.

[13] J. Ruze, "Antenna tolerance theory—A review," *Proc. IEEE*, vol. 54, no. 4, pp. 633–640, Apr. 1966.

[14] A. Babuscia, M. Van de Loo, Q. J. Wei, S. Pan, S. Mohan, and S. Seager, "Inflatable antenna for CubeSat: Fabrication, deployment and resultsof experimental tests," in *Proc. IEEE Aerosp. Conf.*, 2014, pp. 1–12.

[15] W. F. Moulder, R. N. Das, A. C. Maccabe, L. A. Bowen, E. M. Thompson, and P. J. Bell, "Rigid-flexible antenna array (RFAA) for lightweight deployable apertures," in *Proc. 14th Eur. Conf. Antennas Propag. (EuCAP)*, 2020, pp. 1–5.

[16] M. Carvalho, A. D. Johnson, E. A. Alwan, and J. L. Volakis, "Semi-resistive approach for tightly coupled dipole array bandwidth enhancement," *IEEE Open J. Antennas Propag.*, vol. 2, pp. 110–117, 2021.

[17] M. Carvalho and J. L. Volakis, "Performance of partially deployed spaceborne ultra-wideband Miura-ori apertures," *IEEE Open J. Antennas Propag.*, vol. 2, pp. 718–725, 2021.

[18] J. P. Doane, K. Sertel, and J. L. Volakis, "Bandwidth limits for lossless, reciprocal PEC-backed arrays of arbitrary polarization," *IEEE Trans. Antennas Propag.*, vol. 62, no. 5, pp. 2531–2542, May 2014.

[19] H. Wheeler, "Simple relations derived from a phased-array antenna made of an infinite current sheet," *IEEE Trans. Antennas Propag.*, vol. 13, no. 4, pp. 506–514, Jul. 1965.

[20] Y. E. Erdemli, K. Sertel, R. A. Gilbert, D. E. Wright, and J. L. Volakis, "Frequency-selective surfaces to enhance performance of broad-band reconfigurable arrays," *IEEE Trans. Antennas Propag.*, vol. 50, no. 12, pp. 1716–1724, Dec. 2002.

[21] A. O. Bah, P.-Y. Qin, R. W. Ziolkowski, Q. Cheng, and Y. J. Guo, "Realization of an ultra-thin metasurface to facilitate wide bandwidth, wide angle beam scanning," *Sci. Rep.*, vol. 8, p. 4761, Mar. 2018.

[22] D. Pozar, "Analysis of finite phased arrays of printed dipoles," *IEEE Trans. Antennas Propag.*, vol. 33, no. 10, pp. 1045–1053, Oct. 1985.

[23] H. Holter and H. Steyskal, "On the size requirement for finite phased-array models," *IEEE Trans. Antennas Propag.*, vol. 50, no. 6, pp. 836–840, Jun. 2002.

[24] I. Tzanidis, K. Sertel, and J. L. Volakis, "Characteristic excitation taper for ultrawideband tightly coupled antenna arrays," *IEEE Trans. Antennas Propag.*, vol. 60, no. 4, pp. 1777–1784, Apr. 2012.

[25] N. Amitay, V. Galindo, and C. P. Wu, *Theory and Analysis of Phased Array Antennas*. New York, NY, USA: Wiley-Intersci., 1972.

[26] H. S. C. Wang, "Performance of phased array antennas under error conditions," in *Proc. IEEE Aerosp. Appl. Conf.*, 1989, p. 25.

[27] H. S. C. Wang, "Performance of phased-array antennas with mechanical errors," *IEEE Trans. Aerosp. Electron. Syst.*, vol. 28, no. 2, pp. 535–545, Apr. 1992.

MAXENCE CARVALHO (Graduate Student Member, IEEE) was born in Clermont–Ferrand, France, in 1994. He received the M.Sc. degree in aeronautical and spatial telecommunications from l'École National de l'Aviation Civile, Toulouse, France, in 2018. He is currently pursuing the Ph.D. degree with the RFCOM Lab, Florida International University, Miami, FL, USA. His current research interests include ultra-wideband arrays, millimeter-wave antennas for imaging applications, and reconfigurable antennas. He was the Honorable Mention Award recipient in the Student Paper Competition at the 2021 National Radio Science Meeting.

JOHN L. VOLAKIS (Life Fellow, IEEE) was born in Chios, Greece, in May 13, 1956, and immigrated to USA in 1973. He received the B.E. degree *(summa cum laude)* from Youngstown State University, Youngstown, OH, USA, in 1978, and the M.Sc. and Ph.D. degrees from the Ohio State University, Columbus, OH, USA, in 1979, and 1982, respectively. He started his career with Rockwell International North American Aircraft Operations from 1982 to 1984, currently Boeing. In 1984, he was appointed as an Assistant Professor with the University of Michigan, Ann Arbor, MI, USA, becoming a Full Professor in 1994. He also served as the Director of the Radiation Laboratory from 1998 to 2000. From January 2003 to August 2017, he was the Roy and Lois Chope Chair Professor of Engineering with the Ohio State University and served as the Director of the ElectroScience Laboratory from 2003 to 2016. Since August 2017, he has been the Dean of the College of Engineering and Computing and a Professor with the Electrical and Computer Engineering, Florida International University. His publications include eight books, over 440 journal papers and 900 conference papers, 30 book chapters, and 30 patents/disclosures. Among his coauthored books are: *Approximate Boundary Conditions in Electromagnetics* in 1995; *Finite Element Methods for Electromagnetics* in 1998; *Antenna Engineering Handbook* (4th and 5th ed.) in 2007 and 2019; *Small Antennas* in 2010; and *Integral Equation Methods for Electromagnetics* in 2011. Over the years, he carried out research in computational methods, antennas, wireless communications and propagation, electromagnetic compatibility and interference, design optimization, RF materials, multiphysics engineering, millimeter waves, terahertz, and medical sensing. He has graduated/mentored 97 doctoral students/post-docs with 43 of them receiving best paper awards at conferences. Among his awards are: The University of Michigan College of Engineering Research Excellence Award in 1993, the Scott Award from the Ohio State University College of Engineering for Outstanding Academic Achievement in 2011, the IEEE AP Society C-T. Tai Teaching Excellence Award in 2011, the IEEE Henning Mentoring Award in 2013, the IEEE Antennas and Propagation Distinguished Achievement Award in 2014, The Ohio State University Distinguished Scholar Award in 2016, and The Ohio State University ElectroScience Lab. George Sinclair Award in 2017, and the URSI Booker Gold Medal in 2020. His service to Professional Societies include: the 2004 President of the IEEE Antennas and Propagation Society (2004), the Chair of USNC/URSI Commission B (2015–2017), twice the General Chair of the IEEE Antennas and Propagation Symposium, the IEEE APS Distinguished Lecturer, the IEEE APS Fellows Committee Chair, the IEEE-wide Fellows committee Member and associate editor of several journals. He was listed by ISI among the top 250 most referenced authors (2004). He is a Fellow of the Advanced Computational Electromagnetics Society, the American Association for the Advancement of Science, and the National Academy of Inventors in 2021.